Unravelling crystal superstructures and transformations in the La 6-x MoO 12-δ (0.6$\leq$ x $\leq$ 3.0) series. A system with tailored ionic/electronic conductivity.

Adrián López-Vergara, Lucía Vizcaíno-Anaya, Jose Porras-Vázquez, Gianguido Baldinozzi, Lucia dos Santos-Gómez, Jesús Canales-Vázquez, David Marrero-Lopez, Enrique Losilla

Unravelling crystal superstructures and transformations in the $La_{6-x}MoO_{12-\delta}$ ($0.6 \leq x \leq 3.0$) series. A system with tailored ionic/electronic conductivity.

Adrián López-Vergara[1], Lucía Vizcaíno-Anaya[1], José M. Porras-Vázquez[1,*] Gianguido Baldinozzi[2], Lucía dos Santos-Gómez[1], Jesús Canales-Vazquez[3], David Marrero-López[4], Enrique R. Losilla[1].

1 Universidad de Málaga, Dpto. de Química Inorgánica, Cristalografía y Mineralogía 29071-Málaga, Spain
2 SPMS, CNRS, Centrale Supélec, Université Paris-Saclay, F-91190 Gif-sur-Yvette, France
3 Renewable Energy Research Institute, University of Castilla-La Mancha, 02071-Albacete, Spain
4 Universidad de Málaga, Dpto. de Física Aplicada I, 29071-Málaga, Spain

ABSTRACT: Crystalline $La_{6-x}MoO_{12-\delta}$ materials with different lanthanum/molybdenum ratios ($0.6 \leq x \leq 3.0$) have been prepared via a freeze-drying precursor route. The influence of the lanthanum content, sintering temperature and cooling rate on the phase existence range and polymorphism was evaluated. Lanthanum rich compounds present three different polymorphs: a cubic (disordered) fluorite and two complex rhombohedral superstructures related to the fluorite. For the first time, the structural resolution of these rhombohedral superstructures, 7×7×1 and 5×5×1, has been successfully accomplished by neutron powder diffraction and transmission electron microscopy studies. As the La/Mo ratio decreases, the cubic symmetry is stabilized, although a phase transformation from cubic to monoclinic occurs at a low cooling rate. Impedance spectroscopy measurements under different atmospheres (dry and wet N_2 and 5% H_2-Ar) show that all materials exhibit mixed proton-electronic conductivity. The n-type electronic conductivity is attributed to Mo^{6+} reduction and increases for those phases with lower lanthanum content, i.e. for quenched samples, from 5 mS cm^{-1} for $La_{5.4}MoO_{11.1}$ to 9.5 mS cm^{-1} for La_4MoO_9 at 700 ºC in very reducing and wet conditions, which are significantly better than the values published to date for mixed lanthanum tungstates/molybdates. This make these materials potential candidates for hydrogen separation membranes.

1. Introduction

Hydrogen is an excellent energy vector due to its high gravimetric power density compared to fossil fuels.[1-3] It can be obtained via water splitting or, more commonly, via the reforming of hydrocarbons.[4-7] However, the latter procedure leads to a mixture of gases comprised mainly of H_2, CO and CO_2, constraining the separation and purification of H_2, which is performed by a hydrogen separation membrane. Such materials must exhibit high proton conductivity, therefore, state-of-the-art proton conductors, $(Ba,Sr)(Ce,Zr)O_3$ are in principle good candidates for this application.[8-10] However, a major drawback of these materials is their low stability in H_2O and CO_2-rich atmospheres, an important issue when hydrogen is obtained through the reforming of hydrocarbons.[11-12] Over the last years, new candidates for hydrogen separation membranes have arisen, such as those based on lanthanide tungstates/molybdates, $Ln_{6-x}W_{1-y}Mo_yO_{12-\delta}$ (Ln=La-Lu), due to their enhanced phase stability in different environments. Among them, more attention is being drawn to materials where tungsten is complete replaced by molybdenum, due to the higher reducibility of Mo^{6+} compared to W^{6+}, which leads to an increase of the electronic conductivity.[13-16]

Lanthanide molybdates, with general formula $Ln_{6-x}MoO_{12-\delta}$ $0 \leq x \leq 0.6$, present different structures depending on the lanthanide size and the synthetic conditions.[19,20] For instance, $La_{5.4}MoO_{11.1}$ ceramics prepared by the freeze-drying method at 1500 ºC and quenched down to room temperature (RT) crystallize as a simple cubic fluorite. At slower cooling rates, 50 and 0.5 ºC min^{-1}, two rhombohedral polymorphs are isolated. HRTEM studies confirmed that these polymorphs present 7×7×1 (R1) and 5×5×1 (R2) superstructures relative to a basic unit cell with fluorite-type structure. However, due to the complexity and large unit cell volume of these compounds, more than 6500 and 3200 $Å^3$, for R1 and R2, respectively, a complete structural determination was not possible by conventional X-ray diffraction studies.[21]

The symmetry of these compounds can also be tailored by modifying the cationic and anionic frameworks. For instance, Nb-doping on $La_{5.4}MoO_{11.1}$ leads to the stabilization of the R1 polymorph regardless of the preparation conditions, in addition to an improvement of the densification and electrical properties, from 0.17 to 0.44 mS cm^{-1} for $La_{5.4}MoO_{11.1}$ and $La_{5.4}Mo_{0.9}Nb_{0.1}O_{11.05}$, respectively, at 700 ºC in a dry N_2 atmosphere, because of the generation of additional oxygen vacancies.[22] On the other hand, modification of the anionic network

of $La_{5.4}MoO_{11.1}$ and $La_{5.4}Mo_{0.9}Nb_{0.1}O_{11.05}$ by means of fluorination leads to the stabilization of the cubic polymorph at temperatures as low as 1200 ºC, where non-fluorinated samples are a mixture of phases.[23] However, these materials showed a marked decrease of the ionic conductivity under dry/wet N_2 and O_2 atmospheres. For instance, between the non-fluorinated and fluorinated $La_{5.4}Mo_{0.9}Nb_{0.1}O_{11.05}$ samples, both with R1 symmetry, the conductivity decreased from 0.21 to 0.02 mS cm^{-1} at 700 ºC in a dry N_2 atmosphere, due to the filling of the oxide vacancies by fluorine. Moreover, an increase of the n-type electronic conductivity was observed under reducing atmospheres, from 4.0 to 5.3 mS cm^{-1} at 700 ºC, for non-fluorinated and fluorinated $La_{5.4}MoO_{11.1}$, respectively.

The aim of this work is to further explore the phase diagram, crystal structures and electrical properties of lanthanum molybdates with La/Mo molar ratios ($0.6 \leq x \leq 3.0$) and its dependence on different synthesis-sintering conditions.

For the first time, with SAED and the Rietveld refinement of neutron powder diffraction data, the task of solving these complex structures, with 7×7×1 and a 5×5×1 supercells, has been addressed. The symmetry assessment is performed using the superspace formalism,[24] originally developed for incommensurately modulated systems, but often also used to describe complex commensurate modulations.[25]

Finally, microstructural and electrical characterization was carried out by scanning electron microscopy and impedance spectroscopy under different atmospheres, respectively, to evaluate the potential use of these materials as hydrogen separation membrane.

2. Experimental

2.1. Synthesis

Samples with composition $La_{6-x}MoO_{12-\delta}$ (x = 1, 1.5, 2, 2.5 and 3) were prepared by the freeze-drying precursor method using La_2O_3 (99.99%, Aldrich) and MoO_3 (99.5%, Aldrich) as starting reagents, following the synthetic procedure detailed for $La_{5.4}MoO_{11.1}$.[21]

In order to optimize the final sintering temperature, the precursor powders obtained at 800 ºC for 1 h were compacted into pellets of 10 and 1 mm of diameter and thickness, respectively; and sintered between 1000 and 1500 ºC for 1 h with heating and cooling rates of 10 and 5 ºC min^{-1}, respectively. The samples sintered at 1500 ºC were also cooled down at two different rates: quenching (sudden cooling) and 0.5 ºC min^{-1} to study the effect of the sintering treatment on the phase formation and polymorphism. The resulting pellets were ground into fine powders for structural characterization. Hereafter, the $La_{6-x}MoO_{12-\delta}$ samples are labelled as La_{6-x}T-C, where 6-x represents the lanthanum content, T is the sintering temperature and C is the cooling rate.

2.2. Structural and microstructure characterization

The composition and structure of all samples were routinely analyzed by laboratory X-ray powder diffraction (XRPD) using an Empyrean PANalytical diffractometer with $CuK\alpha_{1,2}$ radiation. Structural studies were carried out using a X'Pert Pro MPD (PANalytical) automated diffractometer equipped with a Ge(1 1 1) primary monochromator ($CuK\alpha_1$ radiation) and an X'Celerator detector. The acquisition time was approximately of 4 h over in the 10-120º 2θ range. The phase identification and structural analysis were performed using the X'Pert HighScore Plus and GSAS softwares.[26,27]

Room temperature neutron diffraction (NPD) data were collected in the HRPT diffractometer using the SINQ neutron source at the Paul Scherrer Institut (Villigen, Switzerland). The neutron wavelength, ~1.15 Å, was selected by the 511 reflection of the vertically focusing Ge monochromator and the samples were loaded in a vanadium can. The overall measurement time was 6 h per pattern in order to obtain good statistics over the 2θ range of 13–150° (5–0.6 Å) with a step size of 0.05°.

The crystal structure of the materials was also investigated by selected area electron diffraction (SAED) and high-resolution transmission electron microscopy (HRTEM). The SAED patterns and the corresponding images were recorded using a Jeol JEM 2100 electron microscope operating at 200 kV. TEM images were further analyzed using the Digital Micrograph™ software from Gatan.[28]

The morphology and composition of dense sintered pellets were investigated by field emission scanning electron microscopy (FEI-SEM, Helios Nanolab 650), combined with energy dispersive spectroscopy (EDS, Oxford Instruments). Grain size was estimated from the SEM micrographs, using the linear intercept method with the Estereologia software.[29]

2.3. Electrical characterization

Impedance spectra were acquired using a Solartron 1260 frequency response analyzer in dry and wet (2 vol.% H_2O) N_2 and 5% H_2-Ar. The data were collected in the 0.01 Hz to 1 MHz frequency range with an ac perturbation of 100 mV on cooling, from 750 to 200 °C and a dwell time of 30 min at each measurement temperature. Pt current collectors were formed by coating the pellet surfaces with Pt ink (METALOR® 6082) and then fired at 800 ºC for 1 h in air. The data were analyzed by equivalent circuit models using the ZView program.[30]

3. Results and discussion

3.1. Single phase existence range

XRPD patterns of $La_{6-x}MoO_{12-\delta}$ ($1.0 \leq x \leq 3.0$) calcined at temperatures between 800 and 1500 ºC for 1 h and cooled down at 5 ºC min^{-1} are shown in Figure 1 and S1. Table S1 summarizes the different polymorphs and secondary phases obtained for all compositions at the different sintering temperatures. The as-prepared powders at 800 ºC show broad diffraction peaks for all compositions, attributed to the nanocrystalline nature of the powders, and the patterns can be indexed as a simple cubic fluorite, except for $La_3$800-5, where the reflections are assigned to a monoclinic phase, similar to that recently reported by Dan Vu *et al.* with composition $La_{34}Mo_8O_{75}$.[31] At higher sintering temperatures, different behaviors are observed depending on the La/Mo ratio. For the highest lanthanum content, La_5T-5, and a temperature range of 1000-1500 ºC, single phases are not obtained for 5 ºC min^{-1} cooling rates (Figure 1a). Different phases

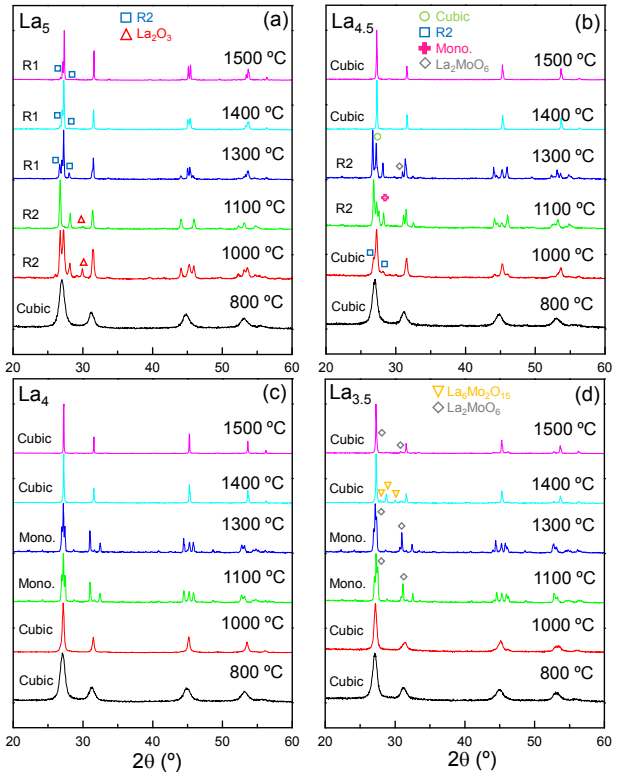

Figure 1. XRPD patterns for $La_{6-x}MoO_{12-\delta}$ (x = 1.0, 1.5, 2.0 and 2.5) heated for 1h at temperatures between 800 and 1500 ºC and cooled down at 5 ºC min^{-1}. The majority phase for each sample is denoted at the bottom left of the diffraction patterns and the minor secondary phases are labelled.

are identified, including R1, R2 and La_2O_3, a similar behaviour to that previously observed for $La_{5.4}MoO_{11.1}$.[21]

In the case of $La_{4.5}$T-5 in the 1000-1300 ºC temperature range, mixtures of a cubic fluorite (isostructural with PDF 00-024-1087), R2, La_2MoO_6 (PDF 01-080-0437) and the monoclinic phase,[31] with composition $La_{34}Mo_8O_{75}$, were identified (Figure 1b). At higher temperatures, i.e. T ≥ 1400 ºC, single phases with a cubic symmetry were obtained. Therefore, lowering the lanthanum content leads to the stabilization of a cubic phase in less demanding synthesis conditions (cooling rate of 5 ºC min^{-1}), in contrast to $La_{5.4}MoO_{11.1}$,[21] which required quenching from 1500 ºC to render the cubic polymorph.

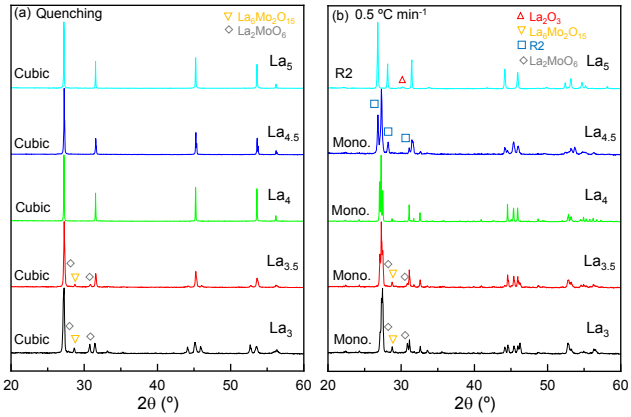

Figure 2. XRPD patterns for $La_{6-x}MoO_{12-\delta}$ (x = 1.0, 1.5, 2.0 and 2.5) heated for 1h at 1500 ºC and cooled down at two different rates: quenching and 0.5 ºC min^{-1}. The majority phase for each sample is denoted at the bottom left of the diffraction patterns and the minor secondary phases are labelled.

In the case of La_4T-5 (Figure 1c), single phases were produced in the whole temperature range; the monoclinic phase formed at temperatures between 1100 and 1300 ºC, whereas a monoclinic→cubic phase transformation is observed above 1400 ºC.

Finally, both $La_{3.5}$T-5 and La_3T-5 present a similar behaviour (Figure 1 and S1) and no single phases could be obtained at any sintering temperature. Mixtures of low La/Mo compositions were identified, such as La_2MoO_6 and $La_6Mo_2O_{15}$ (PDF 00-034-1134), in addition to the monoclinic-and cubic-type structures at low or high temperature, respectively. It has to be noted that the monoclinic phase reported by Dan Vu *et al.*[31] corresponds to a 4.25 La/Mo ratio, therefore it forms in samples with low lanthanum contents, which is not the case of La_5 and $La_{5.4}$.[21]

Figure 2 shows the XRPD patterns of $La_{6-x}MoO_{12-\delta}$ ($1.0 \leq x \leq 3.0$) calcined at 1500 ºC for 1 h and cooled down at two cooling rates, quenching (Figure 2a) and 0.5 ºC min^{-1} (Figure 2b). Table S2 summarizes the phases obtained for all compositions at the two cooling rates. The samples quenched in air are simple cubic fluorites, with the presence of secondary phases, La_2MoO_6 and $La_6Mo_2O_{15}$, for x ≥ 2.5. For the slower cooling rate, 0.5 ºC min^{-1}, in all cases secondary phases were detected, except for La_4 that renders a single phase with monoclinic structure.

The large number of phases that can be isolated as a function of the sintering temperature and the cooling rate can be attributed to the higher ionic radii of lanthanum in an eight-fold coordination (r = 1.16 Å) in comparison to that of molybdenum (r = 1.02 Å), where both occupy the same crystallographic position in a fluorite-type structure. Therefore, as the lanthanum content decreases, single phases gradually tend to cubic symmetry due to the smaller mismatch in the ionic radii of the cationic network. However, when the number of cationic vacancies is too large, the system is no longer stable and phases with low La/Mo ratios are segregated. Moreover, for $La_{5.4}MoO_{11.1}$[21] and La_5, no single phases are obtained at a cooling rate of 5 ºC min^{-1}, and either quenching or slow cooling rates are required to stabilize the different polymorphs, which is further evidence of the instability of systems with high lanthanum contents.

Considering the potential application of these materials at high temperatures, La_4, $La_{4.5}$ and La_5 were annealed at 800 ºC in 5% H_2-Ar for 48 h to evaluate phase stability (Figure S2). All materials retain the original structure, with the exception of $La_4$1400-5, where minor segregations of La_2MoO_6 are detected.

3.2. Crystal structure determination of R1 and R2 polymorphs for $La_{5.4}MoO_{11.1}$

SAED patterns of modulated structures often display a set of strong reflections, from the parent structure, and subsets of weaker reflections corresponding to ordered modulations. In the most general case, the complete sets of main and satellite reflections can be indexed by the reciprocal vector *G* by applying De Wolff's theory within the (3+d)-dimensional superspace group approach.[32]

$$G = ha^* + kb^* + lc^* + m_1q_1 + m_2q_2 + m_3q_3 \quad (1)$$

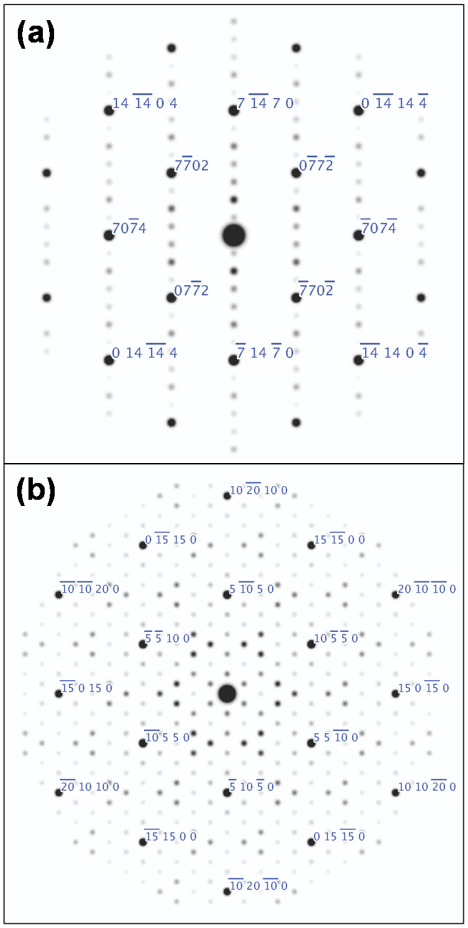

Figure 3. SAED patterns of (a) $La_{5.4}MoO_{11.1}$ with a R1 symmetry in the $[002]_F$ zone axis, where the modulation vectors are of the type $q_{F1} = {}^{1}/_{7}$ (220); and of (b) $La_{5.4}MoO_{11.1}$ with a R2 symmetry in the $[111]_F$ zone axis, where the modulation vectors are of the type $q_{F1} = {}^{1}/_{5}$ (220).

This reciprocal space vector is uniquely identified with 6 integer indices ($hklm_1m_2m_3$). Different satellite orders can be observed, especially when the origin of the modulation is a localized composition fluctuation. The number of independent q_i vectors and their symmetry properties are defined by the superspace group of the crystal. For the R1 and R2 phases, the modulated vectors are commensurate, meaning that they all have a rational relation with the vectors of the average structure.

Figure 3 shows the SAED patterns along the $[002]_F$ and $[111]_F$ zone axes for R1 and R2, respectively. Besides the strong reflections corresponding to the parent fluorite structure, weak but quite sharp satellite reflections are also observed. The parent structure reflections still fulfil the F-lattice extinction rules. These correspond with the strongest reflections observed in the XRPD patterns and they can be indexed according to the parent average fluorite-type structure. There is no apparent violation of the F-lattice rule by the set of weaker reflections. This is an interesting point because a distortion of the lattice would lift the accidental F-type extinctions leaving only the normal site symmetry reflection conditions.

The satellite reflections in both SAED images can be indexed with rational fractions of the parent structure reciprocal vectors. The satellite reflections in Figure 3a corresponding to the $[002]_F$ zone axis appear to be aligned along the [hh0] and [hh̄0] direction and can be indexed as $(\alpha\alpha 0)_F$, $(\alpha\bar{\alpha}0)_F$ with $\alpha=n/7$. This choice of vectors is in good agreement with SAED patterns collected in other zone axes. The satellite reflections in this orientation can be indexed according to a wave vector q_{F1}:

$$q_{F1} = {}^{1}/_{7}\, a_F^* + {}^{1}/_{7}\, b_F^* \qquad (2)$$

At this point it becomes more interesting to leave the conventional fluorite description of Table S3 and use the layered description of Table S4 instead. The direct lattice transformation from the usual fluorite to the trigonal R$\bar{3}$m subgroup is:

$$H = \begin{pmatrix} {}^{\bar{1}}/_{2} & 0 & 1 \\ {}^{1}/_{2} & {}^{\bar{1}}/_{2} & 1 \\ 0 & {}^{1}/_{2} & 1 \end{pmatrix} \qquad (3)$$

This subgroup still enforces the previous F-lattice rule on the main reflections. The change of the point groups also opens the possibility to produce 4 ferroelastic variants that might show up as different domains (90º) in the SAEDs. In the R$\bar{3}$m subgroup, the q_{F1} vector is expressed as $q_{R1} = {}^{1}/_{7}\, b_R^*$. Taking into account the point group $\bar{3}$m, the star of modulation vectors contains 3 branches (e.g., $q_{R2} = {}^{1}/_{7}\, a_R^*$ and $q_{R3} = {}^{\bar{1}}/_{7}\, a_R^* + {}^{\bar{1}}/_{7}\, b_R^*$). The same analysis can be performed on the R2 polymorph, though with $\alpha = {}^{n}/_{5}$.

Using this information, we can build supercells of the average R$\bar{3}$m just multiplying both a_R and b_R by 7 for the R1 and by 5 for the R2 polymorphs.

In the case of the 7×7×1 superstructure the following lattice transformation must be applied to space group G1 = R$\bar{3}$m:

$$P_{R\to R771} = \begin{pmatrix} 7 & 0 & 0 \\ 0 & 7 & 0 \\ 0 & 0 & 1 \end{pmatrix} \qquad (4)$$

This lattice transformation has the effect of generating a space group G_3 for the 7×7×1 supercell that has 1764 symmetry operations. Again, the supplementary elements come from the translation subgroup that now consists of 147 vectors while the point group operations are still the same. The equivalence class of the subgroup R$\bar{3}$m of G_3 consists of 49 cosets to produce the independent atom sites in this large cell. The 20 independent atomic positions of the fluorite structure in the R$\bar{3}$m space group of the 7×7×1 supercell are summarized in Table S5.

In the case of the 5×5×1 superstructure, the first step is to apply the following lattice transformation to the space group G_1 = R$\bar{3}$m:

$$P_{R\to R551} = \begin{pmatrix} 5 & 0 & 0 \\ 0 & 5 & 0 \\ 0 & 0 & 1 \end{pmatrix} \qquad (5)$$

This lattice transformation has the effect of generating a space group G_2 for the 5×5×1 supercell that has 900 symmetry operations. The supplementary elements come from the translation subgroup that now consists of 75 vectors while the point group operations are still the same. The second step of the process involves a proper choice of the symmetry elements of the translation subgroup compatible with the desired final symmetry that is still R$\bar{3}$m because the modulated diffraction pattern still respects the F-center rule. The equivalence class of the

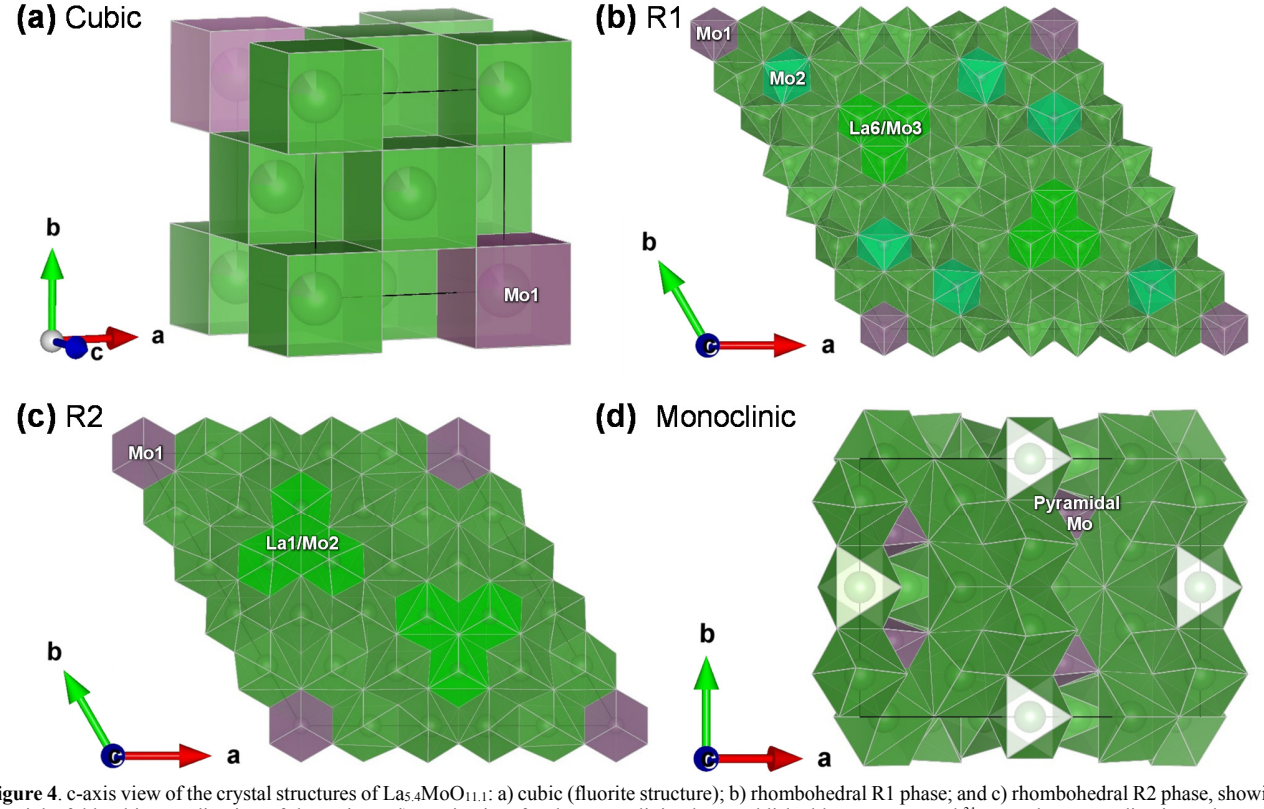

Figure 4. c-axis view of the crystal structures of $La_{5.4}MoO_{11.1}$: a) cubic (fluorite structure); b) rhombohedral R1 phase; and c) rhombohedral R2 phase, showing the eight-fold cubic coordination of the cations. d) c-axis view for the monoclinic phase published by Dan Vu et al.[31] La and Mo coordination spheres are represented by green and purple cubes, respectively. Atomic positions occupied by both lanthanum and molybdenum are in lighter green color.

subgroup $R\bar{3}m$ of G_2 consists of 25 cosets that are used to produce the independent atom sites in this large cell, differing only by translations. The 12 independent atomic positions of the fluorite structure in the $R\bar{3}m$ space group of the 5×5×1 supercell are summarized in Table S6.

All cationic environments in both models possess an 8-fold cubic coordination, where the cubes are sharing edges (Figure 4). Taking into account the absence of secondary phases and the nominal stoichiometry, both models allow the testing of different ordered distributions and occupancies of the metal sites using NPD data and the Rietveld method, where scattering factors from the oxygen atoms are much more significant than in X-ray diffraction.

The deduced theoretical atomic positions (Tables S5 and S6) were used as initial structural models. Parameters such as unit cell, scale factor, background, peak shape coefficients, atomic positions and isotropic displacement parameters were refined. Regarding the type of atom at the metal positions and occupancy factors, a comprehensive analysis was carried out, where each cation was considered to be lanthanum or molybdenum, adjusting its occupancy to reflect the theoretical formula. Then, the occupancies were freely refined and only those scenarios with reasonable M-O distances and good agreement factors were chosen. Finally, oxygen occupancy factors were refined and those very close to the unit were set to 1 and remained fixed.

The final refinement of the R1 phase (s.g.: $R\bar{3}m$, Z = 3, a = 27.9510(9) Å; c = 9.8998(9) Å; V = 6698.1(9) $Å^3$) converged to R_{wp} = 4.09%; R_F = 3.56%. The refined atomic parameters are collected in Table S7, distances in Table S8, a polyhedral view in Figure 4 and the Rietveld plot in Figure 5a. Mo was placed in two positions, one at the origin of coordinates, M1 (0 0 0), a position confirmed by the shorter M-O distances, indicative of a Mo-O bond; and the other one in M5. On the other hand, M2, M3, M4, M6 and M7 were assigned to lanthanum. All these positions (M1-M7) possess a full occupancy (Table S7). The M8 position was splitted between La and Mo, with final occupancy factors of 0.91(3) and 0.09(3), respectively. Therefore, there are eight MO_8 distorted cubes sharing edges (5 of lanthanum, 2 of molybdenum and 1 shared by lanthanum and molybdenum). All of them with reasonable bond distances of 2.02-2.89 Å (La-O) and 2.11-2.60 Å (Mo-O) taking into account the structural complexity, the high number of atoms in the unit cell (402) and the large cell volume, close to 6700 $Å^3$. Finally, it is important to underline that the crystallographic formula obtained from the refinement (Table S7), $La_{5.48}MoO_{11.265}$, is very close to the correctly balanced stoichiometry, $La_{5.48}MoO_{11.22}$, and the nominal one, $La_{5.4}MoO_{11.1}$. Moreover, the crystallographic density (5.834 g cm^{-3}) is quite close with that measured experimentally in dense ceramic pellets, 5.811(3) g cm^{-3}, confirming the validity of the proposed structural model.

The final refinement of the R2 phase (s.g.: $R\bar{3}m$, Z = 3, a = 20.4941(5) Å; c = 9.5183(5) Å; V = 3463.1(8) $Å^3$); converged to R_{wp} = 6.52%; R_F = 3.84%. The atomic parameters are collected in Table S9, distances in Table S10, a polyhedral view in Figure 4 and the Rietveld plot in Figure 5b. In addition to molybdenum in the origin of coordinates (M1), M3, M4 and M5 were assigned to lanthanum with a full occupancy and M2 was splitted between La and Mo, with final occupancies of 0.53(4) and 0.47(4), respectively. There are five MO_8 distorted cubes sharing edges, 3 of lanthanum, 1 of molybdenum and 1 shared

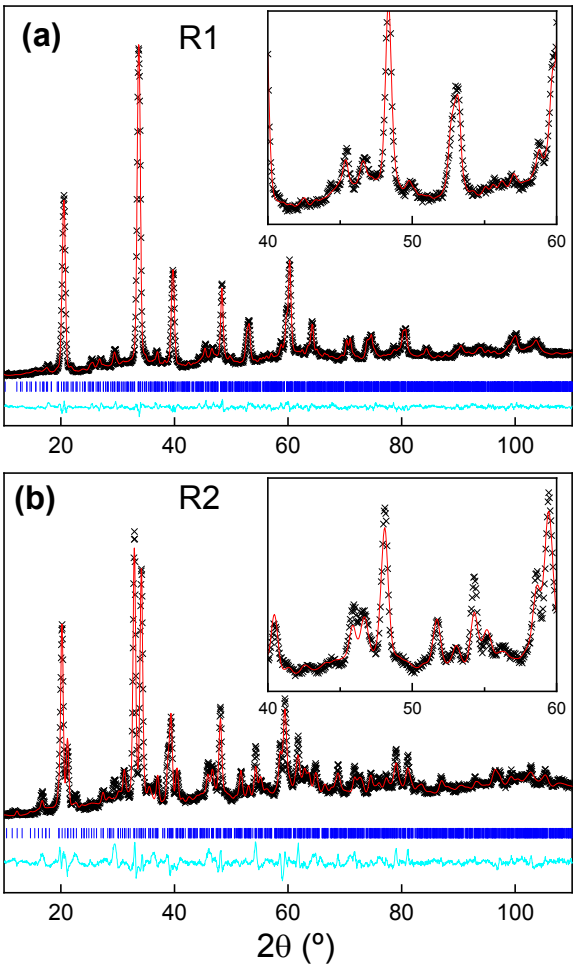

Figure 5. NPD Rietveld plots for $La_{5.4}MoO_{11.1}$: (a) rhombohedral R1 phase and (b) rhombohedral R2 phase using the structural models obtained in this work.

by lanthanum and molybdenum, with reasonable bond distances of 2.16-2.89 Å (La-O) and 2.33-2.55 Å (Mo-O) considering that the structure has 209 atoms and a cell volume close to 3500 $Å^3$. The crystallographic formula, $La_{5.52}MoO_{11.7}$, and density, 5.793 $g{\cdot}cm^{-3}$, obtained from the refinement (Table S9) is very close to the correctly-balanced stoichiometry, $La_{5.52}MoO_{11.28}$, and the experimental density, 5.717(7) $g{\cdot}cm^{-3}$, suggesting the validity of the R2 model.

Both crystal structures have been deposited with the CCDC, with numbers 2011694 and 2011695, for the R1 and R2 models, respectively. It has to be said that, although the formula obtained from the R1 and R2 models are not identical, they are quite close to the theoretical. Finally, despite the accuracy of both models, the broad range in the La(Mo)-O distances might indicate a higher level of disorder in the cationic positions, which is difficult to address with diffraction powder techniques, being necessary the use of single crystal diffraction studies.

Once the cationic distribution of the R1 and R2 phases for $La_{5.4}MoO_{11.1}$ has been defined, it can be understood how the different polymorphs form by tailoring the synthesis-sintering conditions. At very high temperature, 1500 ºC, due to the thermal agitation, lanthanum and molybdenum are disordered in a single crystallographic position M1 (0,0,0), creating a cubic framework that can only be isolated for this composition by quenching. For that symmetry, each La(Mo) is surrounded by eight oxygens at a distance of 2.45 Å. However, when the cooling rate is set to a slower pace, the molybdenum ordering becomes quite evident. For R1, which can be obtained for $La_{5.4}MoO_{11.1}$ at a cooling rate of 50 ºC·min^{-1},[21] or for cation-doped samples, $La_{5.4}Mo_{0.9}Nb_{0.1}O_{11.05}$ and $La_{5.4}Mo_{0.9}Ti_{0.1}O_{11}$, at 5 ºC·$min^{-1}$,[22] all from 1500 ºC, molybdenum/dopant is located in three different positions: the initial one, M1 (0,0,0) and two new ones, M5 ($^1/_7$, $^1/_7$, 0) and M8 ($^2/_7$, $^5/_7$, 0) (Table S5). The slowest cooling rate, 0.5 ºC·min^{-1}, favors the most thermodynamically stable structural arrangement, where one molybdenum remains in the M1 position and the other two converge to the new and final M2 position ($^{-2}/_{15}$, $^{-1}/_{15}$, $^1/_3$) (Table S6). The similarities between the three phases is quite evident, as can be seen in Figure 4a-c, where in any phase transformation there is no breaking of chemical bonds, only slight readjustments to efficiently accommodate the molybdenum. Therefore, each polymorph is convertible into the other two by heating at high temperature and controlling the cooling rate.

3.3. Local and average structure of $La_{6-x}MoO_{12-\delta}$ ($1 \leq x \leq 2$)

The local structure of $La_4$1500-5 and $La_{4.5}$1500-5 were investigated by combined electron diffraction and HRTEM to obtain further insights into the structure. HRTEM images of both samples (Figure 6) reveals a complex texture with domains of cubic and rhombohedral R1 cohabiting. This is confirmed by the electron diffraction patterns calculated in different domains, which reveal different ordering in good agreement with the structural similarities of the polymorphs previously discussed, as the transition between them just requires minor readjustments of the sublattices. However, it must be stressed out that the average symmetry of both samples is cubic, as discussed in section 3.1 by XRPD. No splitting of any X-ray diffraction peak was detected, indicating that the majority of the crystals present a cubic symmetry; however, small reflections are detected in the background, assigned to the rhombohedral microdomains, as can be seen in Figure S3 for $La_{4.5}$1500-5.

The SAED patterns of $La_4$1500-0.5, with a monoclinic structure, were indexed according to the structural model recently proposed by Dan Vu *et al*. (s.g. C12/m1, a= 17.070 Å, b=12.204 Å, c=9.742 Å and β=109.58 º).[31] Figure S4a show the SAED pattern corresponding to the [001] zone axis and intense reflections are observed, which are reminiscent of the cubic fluorite-type structure along the (110) direction. The HRTEM image of $La_4$1500-0.5 (Figure S4b) and the cell parameters of the unit cell is in agreement with the reported monoclinic structure.[31] It should be noticed that this is not a superstructure, unlike the R1 polymorph where 7 weak reflections are observed between the most intense (Figure S4c and d).

Table 1 shows the unit cell parameters and agreement factors obtained by the Rietveld method for $La_{6-x}MoO_{12-\delta}$ ($0.6 \leq x \leq 2$) single phase samples obtained at different cooling rates using the appropriate structural models: i) a simple cubic fluorite; and ii) the structure published by Dan Vu *et al.*[31] for the monoclinic sample. Parameters such as unit cell, scale factor, background, and peak shape coefficients and isotropic displacement parameters were refined. Occupancy factors in each model were conveniently modified to reflect the theoretical stoichiometries. Refinements are quite good with low disagreement factors, R_{wp} and R_F of 5-8 and 2-9 %, respectively

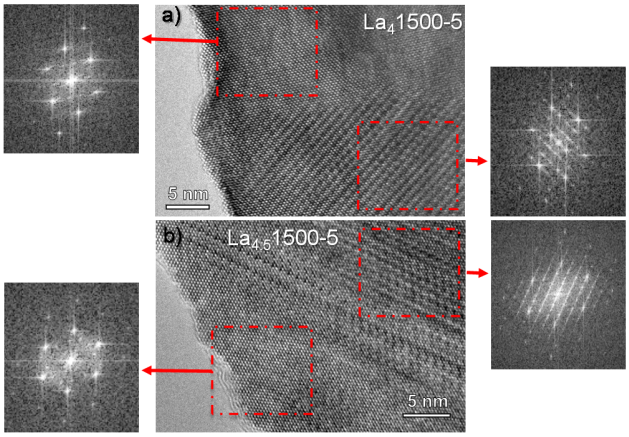

Figure 6. HRTEM images and SAED patterns for (a) $La_4$1500-5 and (b) $La_{4.5}$1500-5.

For $La_4$1500-5 and $La_{4.5}$1500-5 the cubic model adequately adjusts both samples, reflected by the reasonable R_F values (Table 1); however, in the case of the latter is significantly worse, doubling its value, due to the presence of rhombohedral nanodomains as observed by TEM. It must be mentioned that the refinement of $La_{4.5}$1500-5 with a simple rhombohedral phase (Table S4) leads to even worse R_F values (5.21%), indicating that this sample is much closer to a cubic symmetry.

For all quenched samples, the refinements are good using a simple fluorite model (Table 1). $La_{4.5}$1500-Q presents a better R_F value than $La_{4.5}$1500-5 as quenching from 1500 ºC hampers any ordering and distortion in the structure, leading to the highest symmetry.

On the other hand, for the monoclinic sample, despite the profile is adequately fit, the refinement does not lead to good R_F values (Table 1). This is due to the high structural complexity of the sample and hence neutron powder diffraction data are required. This structure possesses 7 independent crystallographic positions for lanthanum (three 8-fold, two 7-fold and two 6-fold) and 1 molybdenum with an unusual oxygen coordination (5-fold), with a pyramidal symmetry. As mentioned in section 3.1, the monoclinic phase is stable between 1100 and 1300 ºC for La_4, which can be transformed into a cubic fluorite by heating at 1500 ºC and cooling by quenching or at 5 ºC min^{-1}. These conditions allow the La/Mo atoms to be completely disordered occupying the M1 position (0,0,0). The relationship between the monoclinic structure and the cubic fluorite is not easy,[31] and in order to make the transition possible and reversible, it is necessary the breaking of at least all non-8-fold polyhedra by heating at 1500 ºC and cooling very slowly at 0.5 ºC min^{-1}, permitting the arrangement of the molybdenum atoms in a pyramidal coordination. A similar behaviour was reported for the formation of the R2 phase for $La_{5.4}MoO_{11.1}$ in the previous section, where only a very slow cooling permitted the stabilization of that symmetry.

For any synthesis-sintering condition, cell parameters show a clear increase as the lanthanum content decreases (Table 1). For instance, in the case of the quenched samples, $La_{5.4}$,[21] La_5, $La_{4.5}$ and La_4, the cell volumes are 45.51(1), 45.54(1), 45.56(1) and 45.58(1) $Å^3$, respectively. This variation is small and complex likely due to the interplay of two factors: (i) the decrease in lanthanum content should slightly contract the structure; and (ii) the decrease in oxygen content that weakens the framework, allowing its expansion, which counterbalances the volume reduction due to lanthanum content. The small differences in cell volumes between samples with the same composition but different sintering conditions might be ascribed to slight deviations in the oxygen contents caused by the different cooling processes.

3.4. Microstructural and electrical characterization

Figure S5 shows SEM micrographs obtained for all single phases sintered at 1500 ºC. The pellets exhibit negligible porosity without visible phase segregations at the grain boundaries, confirming that they are single-phase compounds. These results are further confirmed by EDS analysis (Figure S6) where it can be seen that the samples are homogeneous for lanthanum and molybdenum.

The SEM micrographs were analyzed to evaluate the average grain size (Table 2), which seems to increase slightly with the decrease of the lanthanum content and cooling rate. For instance, the largest average grain size is found for $La_4$1500-0.5, with 20.8 μm, an expected value due to the longer sintering time at high temperatures, allowing a more significant grain growth; and the lowest average grain size is for $La_5$1500-Q, with ~16 μm.

Table 1. Unit cell parameters, cell volumes and agreement factors for $La_{6-x}MoO_{12-\delta}$ (x = 1.0, 1.5 and 2.0) sintered at 1500 ºC and cooled down at different rates (quenching, 5 and 0.5 ºC min^{-1}).

	a (Å)	V/Z ($Å^3$)	R_{wp} (%)	R_F (%)
$La_{5.4}$1500-Q[21]	5.6676(1)	45.51(1)	6.87	3.15
$La_5$1500-Q	5.6686(1)	45.54(1)	6.29	3.99
$La_{4.5}$1500-Q	5.6695(1)	45.56(1)	5.79	3.68
$La_{4.5}$1500-5	5.6605(1)	45.34(1)	8.40	4.86
$La_4$1500-Q	5.6704(1)	45.58(1)	5.51	2.81
$La_4$1500-5	5.6621(1)	45.39(1)	7.58	2.13
$La_4$1500-0.5	a = 17.0611(1) b = 12.2095(1) c = 9.7479(1) β = 109.6(1)º	45.54(1)	6.42	9.19

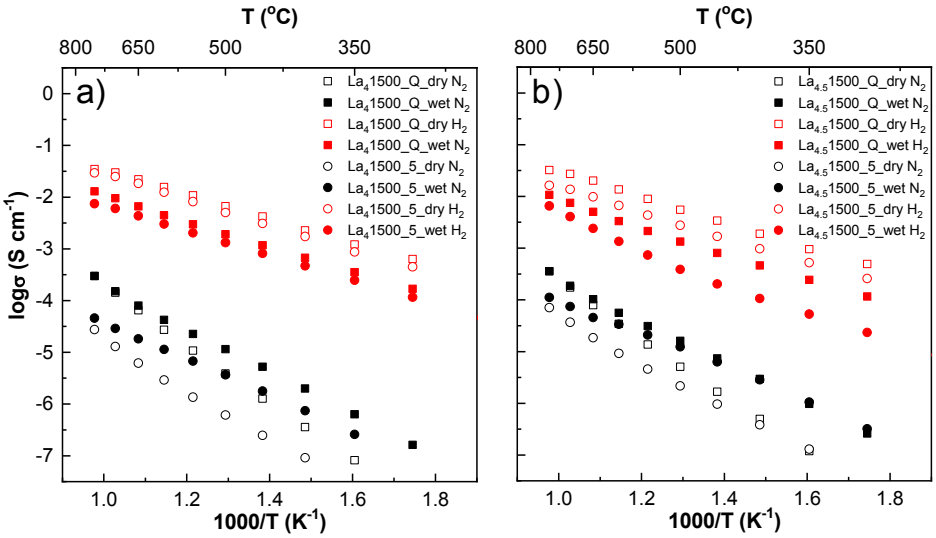

Figure 7. Arrhenius plots for (a) La_4MoO_9 and (b) $La_{4.5}MoO_{9.75}$ sintered at 1500 ºC for 1h and cooled down at different rates under dry and wet N_2 and 5% H_2-Ar atmospheres.

Impedance spectroscopy measurements of the single and stable phases under reducing conditions were carried out under two different flowing atmospheres (dry/wet N_2 and 5% H_2−Ar). Figure S7 shows representative Nyquist plots at 400 ºC for $La_4$1500-Q and $La_{4.5}$1500-Q in dry and wet N_2. Only one contribution at high frequency is detected, which can be fitted with a (RQ) equivalent circuit, where Q is a constant phase element substituting the ideal capacitive element to give a more accurate fit. The associated capacitance of this process is about 10 pF cm^{-1} and can assigned to the bulk conduction. No grain boundary contribution is detected at any sintering temperature or composition, likely due to the large average grain size of the samples and the absence of segregations at the grain limits. Similar spectra are obtained for the remaining samples.

The Arrhenius plots show a very significant enhancement of the conductivity for the samples measured in wet N_2 respect to dry N_2 (Figure 7 and Table 2), indicating an important proton contribution to the conductivity, which is more significant at temperatures lower than 650 ºC, a behaviour already observed for $La_{5.4}MoO_{11.1}$.[21] Notice that this variation is more accused in quenched samples that in those cooled at 5 ºC·min^{-1}. Activation energies regardless of the lanthanum content, present values of ~1.05 eV and 0.83 in dry N_2 and of ~0.80 and ~0.70 eV in wet N_2, respectively. It has to be mentioned that the quenched samples at temperatures higher than 650 ºC, present very similar conductivities in dry and wet atmospheres; however, for those cooled down at 5 ºC min^{-1} there is a slight increase in conductivity at high temperatures in wet N_2 likely due to a higher water absorption.

Moreover, a clear relationship between the conductivity, lanthanum content and cooling conditions can be established from Table 2 and Figure 8. For samples cooled down in the same conditions and measured in the same flowing atmosphere, the conductivity increases with the lanthanum content ($La_{6-x}MoO_{12-\delta}$, x = 0.6), likely due to the fact that an increasing number of oxide vacancies (higher x values, $La_{6-x}MoO_{12-\delta}$, x = 1, 2) disrupt the ionic conduction pathways, hindering the oxide and proton mobility. Importantly, as previously demonstrated, cubic samples always exhibit conductivity values almost one order of magnitude higher than those of rhombohedral or monoclinic polymorphs ($3.2\cdot10^{-2}$ mS·cm^{-1} at 700ºC in air for $La_{38}Mo_8O_{75}$[31]) due to the high symmetry which optimize the ionic trajectories.

Table 2. Average grain sizes and conductivity values at 700 and 400 ºC for $La_{6-x}MoO_{12-\delta}$ (x = 1.5 and 2.0) sintered at 1500 ºC and cooled down at different rates (quenching, 5 and 0.5 ºC min^{-1}).

Sample	Structure	Average grain size (Å)	dry N_2		wet N_2		dry 5%H_2-Ar		wet 5%H_2-Ar	
			$\sigma_{700\,°C}$ (mS/cm)	$\sigma_{400\,°C}$ (mS/cm)	$\sigma_{700\,°C}$ (mS/cm)	$\sigma_{400\,°C}$ (mS/cm)	$\sigma_{700\,°C}$ (mS/cm)	$\sigma_{400\,°C}$ (mS/cm)	$\sigma_{700\,°C}$ (mS/cm)	$\sigma_{400\,°C}$ (mS/cm)
$La_{5.4}$1500-Q[21]	Cubic	15.8	$1.7\ 10^{-1}$	$2.3\ 10^{-3}$	$2.5\ 10^{-1}$	$1.1\ 10^{-2}$	18.0	1.3	5.0	$2.0\cdot10^{-1}$
$La_{4.5}$1500-Q	Cubic	16.1	$1.7\ 10^{-1}$	$5.0\ 10^{-4}$	$1.9\ 10^{-1}$	$2.9\ 10^{-3}$	27.2	1.9	7.5	$4.6\cdot10^{-1}$
$La_{4.5}$1500-5	Cubic	17.0	$3.7\ 10^{-2}$	$3.8\ 10^{-4}$	$7.4\ 10^{-2}$	$2.8\ 10^{-3}$	13.7	$9.7\ 10^{-1}$	4.1	$1.1\cdot10^{-1}$
$La_4$1500-Q	Cubic	19.2	$1.4\ 10^{-1}$	$3.6\ 10^{-4}$	$1.5\ 10^{-1}$	$2.0\ 10^{-3}$	30.0	2.3	9.5	$6.7\cdot10^{-1}$
$La_4$1500-5	Cubic	16.9	$1.3\ 10^{-2}$	$9.1\ 10^{-5}$	$4.6\ 10^{-2}$	$7.4\ 10^{-4}$	24.8	1.7	6.0	$4.7\cdot10^{-1}$
$La_4$1500-0.5	Monoclinic	20.8	$1.8\ 10^{-1}$	$3.5\ 10^{-3}$	$2.6\ 10^{-1}$	$5.0\ 10^{-2}$	6.0	$3.5\ 10^{-2}$	1.6	$3.9\cdot10^{-2}$

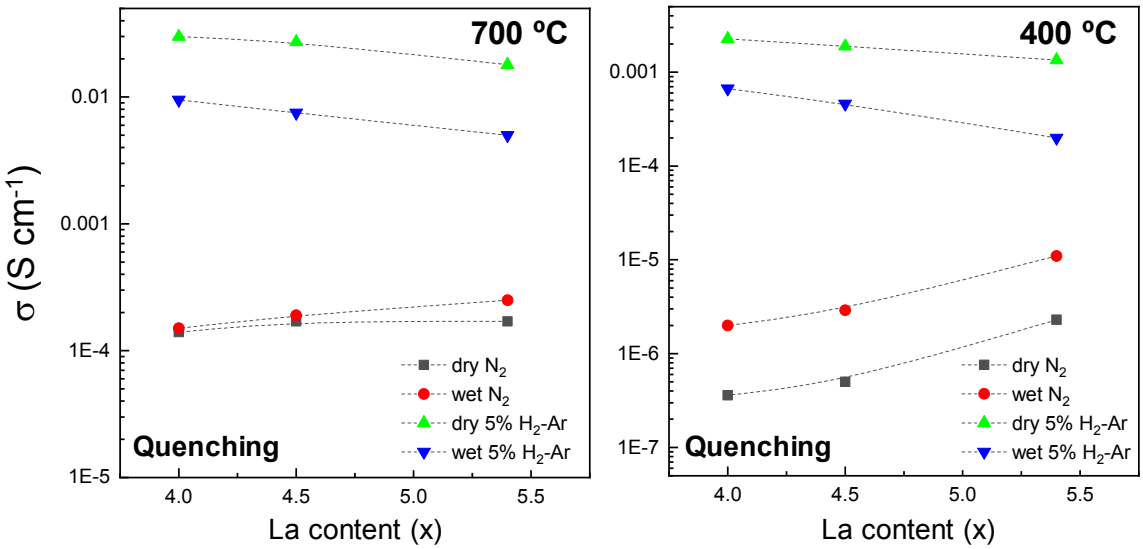

Figure 8. Overall conductivity plots versus lanthanum content at 700 and 400 °C for $La_{6-x}MoO_{12-\delta}$ (x = 0.6, 1.5 and 2) sintered at 1500 ºC for 1 h and cooled down by quenching in dry and wet N_2 and 5% H_2–Ar.

Figure 7 also shows the Arrhenius plots for all the single and redox-stable phases and Table 2 the conductivity values at 700 and 400 ºC. In a 5% H_2-Ar atmosphere (dry and wet) there is a significant increase of the conductivity due to an n-type contribution, caused by a minor reduction of Mo^{6+} to Mo^{5+}, according to the following defect chemistry equation:

$$2Mo_{Mo}^{x} + O_{O}^{x} \rightarrow 2Mo'_{Mo} + V_{O}^{\cdot\cdot} + 1/2\ O_2 \qquad (6)$$

The highest conductivities are observed for the cubic samples. In wet conditions, La4₁500-Q and La4.5₁500-Q present values of 9.5 and 7.5 mS cm^{-1}, respectively, at 700 ºC; and of 6.7 10^{-1} and 4.6 10^{-1} mS cm^{-1}, respectively, at 400 ºC. On the other hand, the lowest conductivity values are observed for La4₁500-0.5, with 1.6 mS cm^{-1} at 700 ºC and 3.9 10^{-2} at 400 ºC, due to the less symmetric monoclinic phase, which hinders the conducting pathways. It should be mentioned that there is a significant difference in conductivity between dry and wet 5% H_2-Ar, where the dry measurements present higher values. This is due to the presence of water in the gas, which leads to a less reducing environment and, therefore, to a smaller n-type electronic contribution in wet conditions.

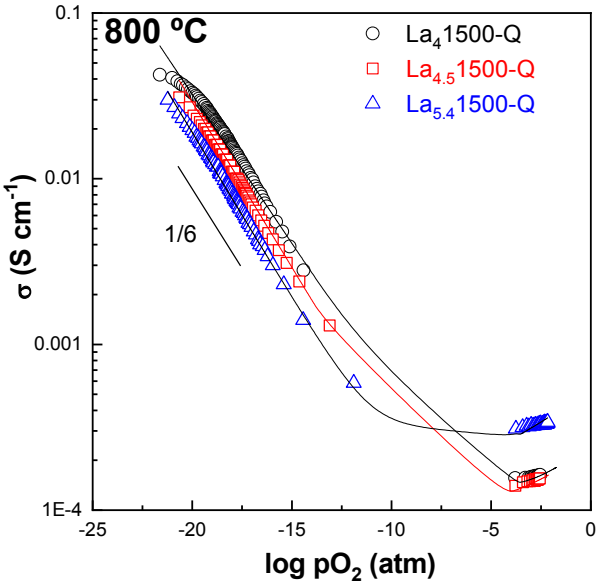

Figure 9. Dependence of the overall conductivity as a function of the oxygen partial pressure at 800 ºC for La4₁500-Q, La4.5₁500-Q and La5.4₁500-Q.[21] The solid line is the fitting with Eq. 7.

It should be noticed that in a reducing atmosphere, for samples obtained in the same conditions, the conductivity increases as the lanthanum content decreases (Figure 8). For instance, the conductivity values in wet conditions for La5.4₁500-Q, La4.5₁500-Q, and La4₁500-Q at 700 ºC are 5.0, 7.5 and 9.5 mS cm^{-1}, respectively. This behaviour is the opposite found in dry/wet N_2 and is likely due to a higher reducibility of the samples with lower La/Mo ratios and the decrease in the cell volumes, which makes the molybdenum atoms to be closer to each other, facilitating the electronic conduction by electron hopping. It is worth mentioning that this increase in conductivity is more significant in the low temperature range, dominated by the proton conduction, when compared to the high temperature region, dominated by the oxide and electron conduction. In addition, a decrease of the activation energies is also observed as the lanthanum content decreases, with values of 0.72, 0.55 and 0.51 eV for La5.4₁500_Q, La4.5₁500_Q and La4₁500_Q, respectively, due to the higher electronic conductivity contribution. Furthermore, no significant differences are observed in the activation energies between dry and wet 5% H_2-Ar, indicating that in those conditions the conduction is dominated by the n-type electronic contribution in the whole temperature range.

The dependence of the conductivity versus the oxygen partial pressure for La4₁500-Q, La4.5₁500-Q and La5.4₁500-Q is plotted in Figure 9. It can be clearly seen an increase in conductivity as the oxygen partial pressure decreases due to a very important n-type electronic contribution, more significant for La4₁500-Q in comparison to La5.4₁500-Q, where the difference between the ionic plateaus and the most reduced points is higher for the former. The n-type branches of the plots show a dependence with the conductivity following the next equation:

$$\sigma = \sigma_o + \sigma_n(pO_2)^{-1/6} + \sigma_P(pO_2)^{1/6} \qquad (7)$$

where σ_o is the ionic conductivity, and σ_n and σ_p are the partial n-type and p-type electronic conductivity, respectively. As can be observed, the n-type contribution is the main conduction mechanism at low oxygen partial pressure and a small p-type contribution is observed at high pO_2 values. These curves clearly confirm that samples with high La-content exhibit higher ionic conductivity with a plateau region at intermediate pO_2 values; however, samples with low La-content exhibits lower ionic conductivity and higher n-type and p-type electronic conductivities.

It has to be said that, to the best of our knowledge, only Mo-doped lanthanum tungstates, with general formula $La_{5.5-x}W_{1-y}Mo_yO_{12-\delta}$ (x = 0 and 0.1, y = 0.2-0.4), have been tested as hydrogen separation membranes.[33,34] However, in this work La41500-Q presents a conductivity of 9.5 mS cm^{-1} at 700 ºC in a 5% H_2-Ar atmosphere, significantly better than $La_{5.5}W_{0.8}Mo_{0.2}O_{11.25}$, with ~ 3 mS cm^{-1} in the same measurement conditions,[35-37] indicating that lanthanum molybdates with low La content are more suitable for hydrogen separation applications. Thus, further studies to explore this point are planned.

4. Conclusions

$La_{6-x}MoO_{12-\delta}$ materials (x = 1, 1.5, 2, 2.5 and 3) were prepared by the freezing-drying method. The structure of the R1 and R2 polymorphs of $La_{5.4}MoO_{11.1}$ has been deduced from HRTEM images and SAED patterns using the superspace formalism and the Rietveld method using neutron powder diffraction data. For R1, a model with eight cationic positions (five of lanthanum, two of molybdenum and one shared by lanthanum and molybdenum) and twelve for oxygen was proposed. The R2 model consisted in five cationic positions (three of lanthanum, one of molybdenum and one shared by lanthanum and molybdenum) and seven for oxygen. Rietveld refinements of both models presented good agreement factors, reasonable bond distances and experimental formula and densities very close to the theoretical ones. Moreover, cation distribution analysis of the cubic, R1 and R2 polymorphs indicated that as the cooling rate decreases the molybdenum atoms order without breaking any chemical bond.

X-ray diffraction studies of compositions with low La/Mo ratio ($x \geq 1.5$) cooled down at 5 ºC min^{-1} from 1500 ºC indicated the formation of samples with a cubic symmetry. However, transmission electron microscopy studies confirmed that the local structure is formed by cubic and rhombohedral (R1) nanodomains that induce certain deviations from the average cubic symmetry. If the cooling is performed at a slower rate, 0.5 ºC min^{-1}, the molybdenum atoms reorder to adopt a pyramidal coordination, leading to a monoclinic structure that requires breaking of most of the coordination polyhedra.

Impedance spectroscopy studies in N_2 atmospheres indicated that the ionic conductivity decreases as the La/Mo ratio becomes lower. However, under reducing conditions (5% H_2-Ar), an increase of the n-type electronic contribution was observed, which makes these materials potential candidates for hydrogen separation membranes.

ASSOCIATED CONTENT

Additional experimental results, including XRPD patterns, SAED and HR-TEM images, SEM micrographs, EDS mappings, Nyquist plots and Tables with XRPD analysis and structural data are supplied as Supporting Information. This material is available free of charge via the Internet at http://pubs.acs.org.

AUTHOR INFORMATION

Corresponding Author

e-mail address: josema@uma.es (José Manuel Porras Vázquez)

Present address: Dpto. de Química Inorgánica, Cristalografía y Mineralogía, Facultad de Ciencias, Campus de Teatinos, Universidad de Málaga, 29071-Málaga, Spain.

Tel: +34 951953298

Author Contributions

The manuscript was written through contributions of all authors. / All authors have given approval to the final version of the manuscript.

Funding Sources

This work was supported by Ministerio de Ciencia, Innovación e Universidades through the RTI2018-093735-B-I00 and MAT2016-77648-R and Junta de Andalucía through UMA18-FEDERJA-033 research grants (Spain). J.M.P.-V. thanks the University of Málaga for his funding. A. L.-V. thanks Junta de Andalucía and the European Social Fund for his Young Researcher Contract (UMAJI35).

ACKNOWLEDGMENT

We would like to thank the SINQ facility (Paul Scherrer Institute) for the NPD time and Denis Sheptyakov for his help during the NPD experiments.

REFERENCES

[1] Midilli, A.; Ay, M.; Dincer, I.; Rosen, M. A. On hydrogen and hydrogen energy strategies II: future projections affecting global stability and unrest. *Renewable Sustainable Energy Rev.* **2005**, *9*, 273−287.

[2] Winter, C. J. Hydrogen energy-Abundant, efficient, clean: a debate over the energy-system-of-change. *Int. J. Hydrogen Energy* **2009**, *34*, S1−S52.

[3] Momirlan, M.; Veziroglu, T. N. The properties of hydrogen as fuel tomorrow in sustainable energy system for a cleaner planet. *Int. J. Hydrogen Energy* **2005**, *30*, 795−802.

[4] Hickman, D. A.; Schmidt, L. D. Production of syngas by direct catalytic oxidation of methane. *Science* **1993**, *259*, 343−346.

[5] Kopyscinski, J.; Schildhauer, T. J.; Biollaz, S. M. A. Production of synthetic natural gas (SNG) from coal and dry biomass – A technology review from 1950 to 2009. *Fuel* **2010**, *89*, 1763−1783.

[6] Cortright, R. D.; Davda, R. R.; Dumesic, J. A. Hydrogen from catalytic reforming of biomass-derived hydrocarbons in liquid water. *Nature* **2002**, *418*, 964−967.

[7] Khaselev, O.; Turner, J. A. A monolithic photovoltaic photoelectrochemical device for hydrogen production via water splitting. *Science* **1998**, *280*, 425−427.

[8] Hamakawa S.; Hibino T.; Iwahara H. Electrochemical hydrogen permeation in a proton-hole mixed conductor and its application to a membrane reactor. *J Electrochem Soc*. **1994**, *141*, 1720–1725.

[9] Guan J.; Dorris, S. E.; Balachandran U.; Liu, M. L. Transport properties of $SrCe_{0.95}Y_{0.05}O_{3-\delta}$ and its application for hydrogen separation. *Solid State Ionics* **1998**, *110*, 303–310.

[10] Zhang K.; Sunarso J.; Pham G.; Wang S.; Liu S. External short circuit-assisted proton conducting ceramic membrane for H_2 permeation. *Ceram Int*. **2014**, *40*, 791–797.

[11] Ryu, K. H.; Haile, S. M. Chemical stability and proton conductivity of doped $BaCeO_3$-$BaZrO_3$ solid solutions. *Solid State Ionics* **1999**, *125*, 355−367.

[12] Zakowsky, N.; Williamson, S.; Irvine, J. T. S. Elaboration of CO_2 tolerance limits of $BaCe_{0.9}Y_{0.1}O_{3-\delta}$ electrolytes for fuel cells and other applications. *Solid State Ionics* **2005**, *176*, 3019−3026.

[13] Escolástico, S.; Solís, C.; Serra, J. M. Study of hydrogen permeation in $(La_{5/6}Nd_{1/6})_{5.5}WO_{12-\delta}$ membranes. *Solid State Ionics* **2012**, *216*, 31−35.

[14] Gil, V.; Gurauskis, J.; Kjølseth, C.; Wiik, K.; Einarsrud, M.-A. Hydrogen permeation in asymmetric $La_{28-x}W_{4+x}O_{54+3x/2}$ membranes. *Int. J. Hydrogen Energy* **2013**, *38*, 3087−3091.

[15] Escolástico, S.; Solís, C.; Scherb, T.; Schumacher, G.; Serra, J. M. Hydrogen separation in $La_{5.5}WO_{11.25-\delta}$ membranes. *J. Membr. Sci*. **2013**, *444*, 276−284.

[16] Vøllestad, E.; Vigen, C. K.; Magrasó, A.; Haugsrud, R. Hydrogen permeation characteristics of $La_{27}Mo1.5W_{3.5}O_{55.5}$. *J. Membr. Sci*. **2014**, *461*, 81−88.

[17] Chen, Y.; Liao, Q.; Li, Z.; Wang, H.; Wei, Y.; Feldhoff, A.; Caro, J. A CO_2-stable hollow-fiber membrane with high hydrogen permeation flux. *AIChE J*. **2015**, *61*, 1997−2007.

[18] Polfus, J. M.; Xing, W.; Fontaine, M.-L.; Denonville, C.; Henriksen, P. P.; Bredesen, R. Hydrogen separation membranes based on dense ceramic composites in the $La_{27}W_5O_{55.5}$-$LaCrO_3$ system. *J. Membr. Sci*. **2015**, *479*, 39−45.

[19] Shlyakhtina, A. V.; Savvin, S. N.; Lyskov, N. V.; Kolbanev, I. V.; Karyagina, O. K.; Chernyak, S. A.; Shcherbakova, L. G.; Núñez, P. Polymorphism in the Family of $Ln_{6-x}MoO_{12-\delta}$ (Ln= La, Gd - Lu; x = 0, 0.5) Oxygen Ion- and Proton-Conducting Materials. *J. Mater. Chem. A* **2017**, *5*, 7618−7630.

[20] Savvin, S. N.; Shlyakhtina, A. V.; Borunova, A. B.; Shcherbakova, L.G.; Ruiz-Morales, J.C.; Núñez, P. Crystal structure and proton conductivity of some Zr-doped rare-earth molybdates, *Solid State Ionics* **2015**, *271*, 91–97.

[21] López-Vergara, A.; Porras-Vázquez, J. M.; Infantes-Molina, A.; Canales-Vázquez, J.; Cabeza, A.; Losilla, E. R.; Marrero-López, D. Effect of Preparation Conditions on the Polymorphism and Transport Properties of $La_{6-x}MoO_{12-\delta}$ ($0 \leq x \leq 0.8$). *Chem. Mater*. **2017**, *29*, 6966−6975.

[22] López-Vergara, A.; Porras-Vázquez, J. M.; Vøllestad, E.; Canales-Vázquez, J.; Losilla, E. R.; Marrero-López, D. Metal-Doping of $La_{5.4}MoO_{11.1}$ Proton Conductors: Impact on the Structure and Electrical Properties, *Inorg. Chem*. **2018**, *57*, 12811−12819.

[23] López-Vergara, A.; Bergillos-Ruiz, M.; Zamudio-García, J.; Porras-Vázquez, J. M.; Canales-Vazquez, J.; Marrero-López, D.; Losilla, E. R. Synergic Effect of Metal and Fluorine Doping on the Structural and Electrical Properties of $La_{5.4}MoO_{11.1}$-Based Materials, *Inorg. Chem*. **2020**, *59*, 1444−1452.

[24] Janssen, T.; Janner, A.; Looijenga-Vos, A.; de Wolff, P. M. Incommensurate and commensurate modulated structures. In *International Tables for Crystallography vol C*; Wilson, A. J. C., Ed. The International Union of Crystallography and Kluwer Academic Publishers: Dordrecht, 1992; pp. 797−803.

[25] Perez-Mato, J. M.; Madariaga, G.; Zuniga, F. J.; Garcia Arribas, A. On the structure and symmetry of incommensurate phases. A practical formulation. *Acta Cryst. A* **1987**, *43*, 216−226.

[26] X'Pert HighScore Plus Program, Version 3.0e; PANalytical B.V.: Amelo, The Netherlands, 2012.

[27] Larson, A. C.; von Dreele, R. B. GSAS Program; Report LA-UR-86748; Los Alamos National Lab, 1994.

[28] Digital Micrograph, Version 3.22.1461.0; Gatan: Pleasanton, CA.

[29] Abrantes, J. C. C. Estereologiá, UIDM, ESTG; Polytechnic Institute of Viana do Castelo: Viana do Castelo, Portugal, 1998.

[30] Johnson, D. ZView: A Software Program for IES Analysis, Version 2.9c; Scribner Associates, Inc.: Southern Pines, NC, 2005.

[31] Dan Vu. T.; Krichen, F.; Barré, M.; Coste, S.; Jouanneaux, A.; Suard, E.; Fitch, A.; Goutenoire, F. Ab-initio structure determination of $La_{34}Mo_8O_{75}$ using powder X-ray and neutron diffraction data. *Cryst. Growth Des*. **2019**, *19*, 6074−6081.

[32] de Wolff, P. M. Symmetry operations for displacively modulated structures. *Acta Cryst. A* **1977**, *33*, 493−497.

[33] Chen, Y.; Liao, Q.; Li, Z.; Wang, H.; Wei, Y.; Feldhoff, A.; Caro, J. A CO_2-stable hollow-fiber membrane with high hydrogen permeation flux. *AIChE J*. **2015**, *61*, 1997−2007.

[34] Vøllestad, E.; Vigen, C. K.; Magrasó, A.; Haugsrud, R. Hydrogen permeation characteristics of $La_{27}Mo_{1.5}W_{3.5}O_{55.5}$. *J. Membr. Sci*. **2014**, *461*, 81−88.

[35] Amsif, M.; Magrasó, A.; Marrero-López, D.; Ruiz-Morales, J. C.; Canales-Vázquez, J.; Núñez, P. Mo-substituted lanthanum tungstate $La_{28-y}W_{4+y}O_{54+\delta}$: a competitive mixed electron−proton conductor for gas separation membrane applications. *Chem. Mater*. **2012**, *24*, 3868−3877.

[36] Seeger, J.; Ivanova, M. E.; Meulenberg, W. A.; Sebold, D.; Stöver, D.; Scherb, T.; Schumacher, G.; Escolástico, S.; Solís, C.; Serra, J. M. Synthesis and Characterization of Nonsubstituted and Substituted Proton-Conducting $La_{6-x}WO_{12-y}$. *Inorg. Chem*. **2013**, *52*, 10375−10386.

[37] Magrasó, A. Transport number measurements and fuel cell testing of undoped and Mo-substituted lanthanum tungstate. *J. Power Sources* **2013**, *240*, 583−588.